Results in Engineering 30 (2026) 110777



Contents lists available at ScienceDirect

Results in Engineering

journal homepage: www.sciencedirect.com/journal/results-in-engineering



Research paper

Early detection of thermal fatigue damage using ultrasonic shear waves



Laurence Clarkson, Frederic Cegla *

Non-Destructive Evaluation Group, Department of Mechanical Engineering, Imperial College London, London, SW7 2AZ, UK

ARTICLE INFO

Keywords:
High-cycle thermal fatigue
Ultrasonic monitoring
Temperature measurements
304 Stainless steel
Fatigue cracking

ABSTRACT

Thermal fatigue is a damage mechanism which can occur in a range of engineering contexts. For example, high-cycle thermal fatigue (HCTF) can occur in nuclear power plant (NPP) piping where turbulent fluid mixing produces rapid, localised temperature fluctuations. If undetected, the accumulated damage may initiate cracks, as highlighted by the Civaux 1 reactor incident in 1998. Existing monitoring methods rely on external temperature sensors, but fail to capture high-frequency (1 Hz) fluctuations because the pipe wall acts as a low-pass thermal filter. A non-invasive technique for HCTF monitoring that overcomes the thermal filtering effect is desirable given the potentially deadly repercussions of cracks in NPPs.

Ultrasonic velocity and attenuation are known to be sensitive to thermal fatigue. However, experimental studies to date were limited to post-fatiguing measurements. This study investigated whether thermal-fatigue-induced changes in velocity and attenuation could be detected during thermal cycling using a permanently installed transducer. Cyclic thermal transients of up to 600 °C were used to induce (low-cycle) thermal fatigue in three samples of austenitic stainless steel, with two taken to failure (cracking). Fatigue damage was confirmed using electron backscatter diffraction (EBSD), and shear and Rayleigh wave measurements.

The ultrasonic shear velocity decreased as the number of thermal transients experienced by each sample increased, as expected. However, the relationship between the magnitude of the decrease and the number of transients was not straightforward. The attenuation increased following crack initiation; ≈ 30% and ≈ 150% for shear polarisation parallel and perpendicular to the (expected) crack direction, respectively. Further validation on a larger sample set, and under representative conditions and geometries is required. However, these results demonstrate the potential for HCTF monitoring using changes in velocity and attenuation.

1. Introduction

On the 12th May 1998, a leak occurred at EDF's Civaux 1 (N4 series) pressurised water reactor. The leak caused radioactive steam to be released into the reactor building at a rate of approximately 30 $m^3\,h^{-1}$ [1,2]. Investigations revealed that the leak originated from a 180 mm longitudinal crack initiated on the inner surface of a pipe elbow extrados within line A of the residual heat removal system (RHRS) [3]. The pipe elbow was located immediately downstream of a mixing zone T-junction whose hot and cold legs carried water at 180 and 20 °C, respectively.

The failure at Civaux was found to be caused by HCTF, which occurs when temperature fluctuations induce cyclic thermal stresses that fall within the elastic regime due to a mismatch in deformation of the hot and cold parts of the component. Repeated exposure to these thermal stresses can lead to crack initiation, propagation, and ultimately, component failure [4]. Austenitic stainless steels are particularly susceptible to HCTF due to a combination of low thermal conductivity and high thermal expansion coefficient [5]. This is concerning because austenitic stainless steels (SSs) are used throughout NPPs [6,7].

Significant research was performed to identify the conditions under which mixing zone HCTF occurs [8]. It was concluded that the HCTF at Civaux 1 was caused by the turbulent mixing of the fluids from each branch of the T-junction [9–11]. Further studies found that HCTF is most severe for temperature fluctuations with frequencies around 0.1–1 Hz and differences > 50 °C [12–14]. In fact, HCTF was overlooked during the design of the N4 reactor series [1,8,15] because the contemporary design standards only considered mechanical fatigue failure [1]. Furthermore, HCTF is an ongoing issue as thermal fatigue cracks at the Penly 2 and Cattenom 3 reactors were reported on the 6th March 2023 [16,17]. Therefore, a monitoring-based (rather than inspection-based) method to track progression of HCTF within NPPs is desirable.

* Corresponding author.
E-mail address: f.cegla@ic.ac.uk;f.cegla@imperial.ac.uk (F. Cegla).

https://doi.org/10.1016/j.rineng.2026.110777
Received 6 January 2026; Received in revised form 21 April 2026; Accepted 28 April 2026
Available online 2 May 2026
2590-1230/© 2026 The Authors. Published by Elsevier B.V. This is an open access article under the CC BY license (http://creativecommons.org/licenses/by/4.0/).

Abbreviations

EBSD	Electron backscatter diffraction
EMAT	Electromagnetic acoustic transducer
FAMOSi	Integrated Fatigue Monitoring System
FSI	Flow-Structure Interaction
HCTF	High-cycle thermal fatigue
NPP	Nuclear power plant
OCLC	Orthogonal co-located coils
OPS	Oxide polishing suspension
RHRS	Residual heat removal system
SHM	Structural health monitoring
SS	Stainless steel
TOF	Time-of-flight
TOP	Ternary odd-periodic

1.1. Ultrasound for structural health monitoring

structural health monitoring (SHM) has become an important method for detecting early indicators of damage and ensure the safety of infrastructure [18,19]. SHM systems aim to provide continuous or periodic assessment of structural integrity through integrated sensing, data acquisition, and damage characterisation [20]. In recent years, the development of permanently installed sensing systems has enabled in-situ and real-time monitoring of structural components without interrupting service conditions [21]. These types of systems allow for continuous tracking of damage progression, making them especially suitable for harsh environments involving cyclic loading and temperature variations.

Both bulk and guided wave ultrasonic-specific SHM has been the topic of significant research efforts [18,22–24]. Despite these advances, challenges remain in applying ultrasonic SHM techniques to complex degradation mechanisms such as thermal fatigue, where coupled effects influence material properties and signal interpretation. Therefore, further investigation into ultrasonic monitoring methods under thermal fatigue conditions is of significant importance for engineering applications.

2. Article structure

The remainder of this article is structured as follows. Section 3 introduces existing methods for HCTF monitoring, based on external temperature and ultrasound measurements, as well as their limitations. Section 4 describes the experimental setup used to induce thermal fatigue in samples of austenitic SS. The methods to confirm the presence of thermal fatigue (shear wave velocity and attenuation maps, and Rayleigh wave velocity measurements) are also described. Section 5 presents the results and a discussion of the findings. Finally, the main findings of the presented work are summarised in Section 6.

3. Monitoring high-cycle thermal fatigue

From 2000, EDF introduced a reactor-wide policy governing the operation, in-service monitoring and replacement of so-called mixing zones. The policy stipulates that ultrasonic inspection should be performed on any region of the RHRS exposed to large temperature differences for a cumulative period of 450 hours [1,8]. However, given the inconvenience of such inspections (e.g., infrequency and hazardous conditions), alternative solutions have been explored.

3.1. Temperature-based methods

Since HCTF is driven by thermal gradients, assessment of its progression by resolving these gradients directly would be ideal [14,25], e.g., embedded thermocouples [26] and inversion of external thermocouple data, e.g., the integrated Fatigue Monitoring System (FAMOSi) [27,28]. However, the former is unsuitable for thin-walled pipes and the invasive nature will accelerate component failure [29] whilst the latter is fundamentally insensitive to thermal fluctuations above 1 Hz [27,30] due to the effective thermal low-pass filtering, especially in austenitic SSs [12,31,32].

3.2. Ultrasonic-based methods

A complementary method that uses the relative change in ultrasonic time-of-flight (TOF) has been investigated to overcome the thermal filtering limitations of the FAMOSi [30]. The sensitivity of this method was demonstrated under realistic HCTF conditions in austenitic SS at the Flow-Structure Interaction (FSI) test rig [33]. The maximum detectable fluctuation frequency determined to be 1 Hz for a fluctuation amplitude $> 130\,^{\circ}\mathrm{C}$ and the hot branch temperature $> 150\,^{\circ}\mathrm{C}$, which are comparable to the HCTF conditions at Civaux 1. This was achieved using shear horizontal (SH) waves travelling at 45° to the pipe surface normal generated using electromagnetic acoustic transducers (EMATs). However, converting the TOF information into a (multi-axial) stress state was not addressed in [30], meaning the fatigue state of a component cannot be estimated.

It has been shown that ultrasonic velocity and attenuation are both sensitive to fatigue damage theoretically [34–37] and verified experimentally by Sarris et al. [38,39]. The change in ultrasonic properties is due to the increase in dislocations. Hence, this approach is expected to be applicable in both high- and low-cycle fatigue contexts. Therefore, Sarris proposed monitoring fatigue by comparing ultrasonic velocity maps obtained before and during service [40]. By tracking changes relative to the initial state, knowledge of component thickness is not needed (assuming corrosion/erosion does not occur).

However, this approach has two main limitations. Firstly, the expected velocity change is small even for highly fatigued components: ≈ 0.3% reduction in shear wave speed for a thermally-fatigued austenitic SS plate with 86% of its fatigue life consumed. This reduction is equivalent to a uniform temperature difference of $\approx 12\,^{\circ}\mathrm{C}$ based on Eq. (1), which describes the shear wave velocity in 304 austenitic SS as a function of temperature. In Eq. (1), $V_{\mathrm{Sh,\,304}}$ and T have units of $\mathrm{m\,s^{-1}}$ and °C, respectively. The values for the coefficients in Eq. (1) were taken from [41]: $P_2 = -10^{-5}\ \mathrm{m\,s^{-1}\,{}^{\circ}C^{-2}}$, $P_1 = -0.775\ \mathrm{m\,s^{-1}\,{}^{\circ}C^{-1}}$ and $P_0 = 3188.73\ \mathrm{m\,s^{-1}}$.

$$v_{\mathrm{Sh,\,304}}(T) = P_2 T^2 + P_1 T + P_0 \tag{1}$$

Therefore, the velocity maps would need to be obtained during (infrequent) plant shutdowns for consistent thermal conditions, although identical conditions are unlikely to be guaranteed, limiting suitability for continuous monitoring.

Secondly, while steel composition is known to affect the change in ultrasonic velocity due to fatigue, the exact relationship remains unclear. This implies that composition-specific correlations between velocity change and fatigue damage are required for every component to accurately predict the remaining life [39].

Furthermore, the velocity maps for the plates presented by Sarris et al. were obtained after the fatiguing process only [38,39]. The healthy/pre-fatigue data were obtained from a separate, unfatigued plate. This article aims to extend the work of Sarris et al. [38–40] by investigating whether changes in ultrasonic velocity and attenuation regularly measured by a permanently installed transducer during the fatiguing process can provide an early indication of thermal fatigue damage.

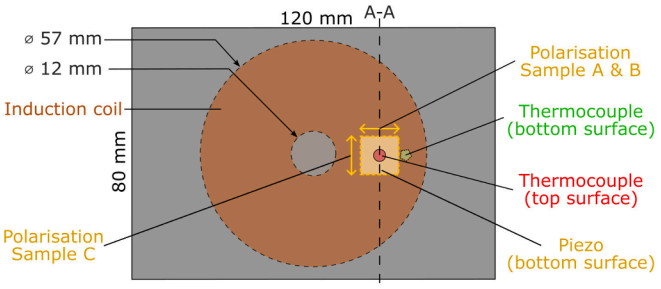
4. Experimental methods

4.1. Thermal fatigue rig

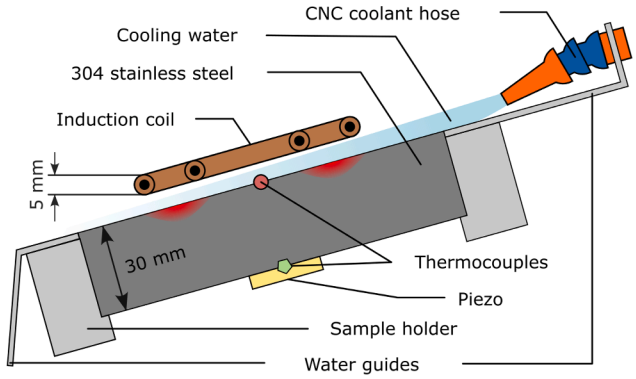
Three samples of 304 SS, A–C, (≈ 120 mm × 80 mm × 30 mm) underwent a non-standard fatigue test comprising non-homogeneous cyclic

Table 1
Details of the thermally fatigued samples. Uncertainties of the mean thicknesses are the standard deviation of the measurements. Cycles (Number of applied transients) marked with a † denote samples taken to failure (Cracking).

Sample ID	Thickness [mm]	Transient amplitude [°C]	Cycles
A	30.62 ± 0.02	≈ 150–350	4377
B	30.63 ± 0.02	≈ 480–580	7850†
C	29.77 ± 0.10	≈ 480–580	1064†



(a) Top view, sample holder and cooling system omitted. The double-headed arrows denote the shear wave polarisation of each piezoelectric crystal.



(b) Cross-sectional view along line A-A of Fig. 1a. The holder and cooling system are included. The red regions below the induction coil represent the heating due to induction.

Fig. 1. Schematic diagrams of the key components of the experimental setup.

thermal transients applied to one surface. Details of each sample and test are given in Table 1. The thicknesses in Table 1 are the average of 12 locations measured using a micrometre. It should be noted that the thermal transients in this work were significantly larger than those that caused the Civaux 1 incident. The larger transients were used to achieve thermal fatigue damage in a reasonable time frame by inducing low-cycle thermal fatigue (rather than HCTF).

Fig. 1 illustrates the experimental setup used to thermally fatigue the samples. The samples were loaded by applying non-homogeneous thermal transients to the 'top' surface of the samples using an induction heater and spiral coil (Powerduction 160LG and L180, GYS, France). The samples were not mechanically loaded and were minimally constrained in the directions normal to the heated surface by the holder, which is illustrated in Fig. 1(b). This method of fatiguing follows the fatigue process in [39].

The induction coil creates an annular heated region as shown in Fig. 2 which illustrates the normalised temperature distribution, T^*, at 0.5 s intervals. The temperatures were measured using a line of K-type thermocouples spot-welded spaced at 3 mm intervals along the centre line of the 80 mm edge, which is labelled in Fig. 1(a). The temperatures were normalised using Eq. (2) where T_{max} and T_{min} are the maximum and minimum temperatures, respectively. The (normalised) error bars

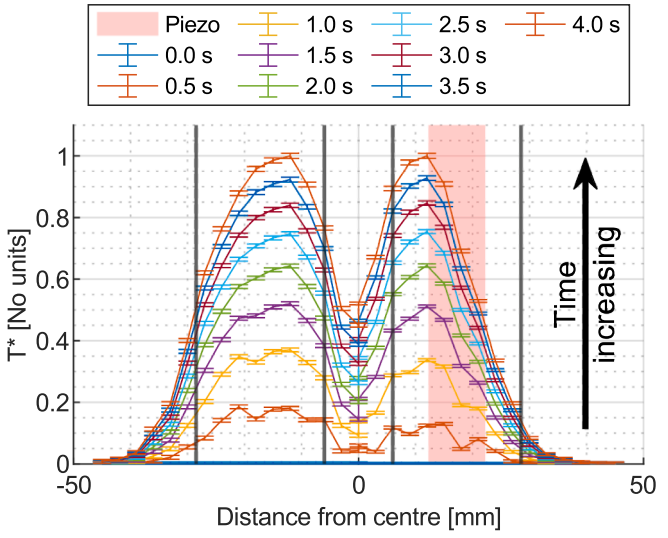


Fig. 2. Spatio-temporal variation in normalised temperature due to the induction heating setup used to thermally fatigue the samples. The vertical black lines denote the approximate bounds of the induction coil. The shaded region defines the bounds of the piezoelectric crystal.

denote the larger of ±2.2 °C and ± 0.75% of the values [42].

$$T^* = \frac{T - T_{min}}{T_{max} - T_{min}} \quad (2)$$

After heating, the top surface was quenched using water delivered by a Rule iL280 water pump (Xylem, United States) and a CNC coolant nozzle. The water was cooled using a 5 kW water chiller (CW-5200TH, Megacold). Before quenching, the sample was retracted using a motorised linear stage. The opposing ('bottom') surface was cooled using a 12 V computer fan. An Arduino Uno (Arduino, Italy) was used for hardware control. The thermal cycling was delayed by 30 s at the start of each run to obtain ultrasonic and temperature data under uniform temperature conditions. Cycling was paused for 15 min after every 90 transients to prevent overheating.

4.2. Data acquisition

Pulse-echo ultrasonic A-scans were obtained using 10 mm × 10 mm × 0.5 mm shear wave piezos (CTS Corporation, USA) bonded to the bottom surface of the samples using 832HT high-temperature epoxy (MG Chemicals, Canada). An A-scan represents an ultrasonic signal with signal amplitude on the vertical axis and time on the horizontal axis [43]. The piezos were excited using a 5-cycle, 1.75 MHz Hann-windowed ternary odd-periodic (TOP) sequence [44] and acquired (without amplification) using a Handyscope HS5 (TiePie) sampling at 50 MHz. The excitation voltage was 4 V. The TOF was calculated using parabolic interpolation of the auto-correlation of the A-scans [45].

Temperature measurements were obtained using N-type thermocouples (spot-welded to the top and bottom surfaces of each sample) and two independent TC-08 data loggers (Pico Technology Ltd., UK). The repeatability of N-type thermocouples is the larger of ±2.2 °C and ± 0.75% of the values. Fig. 3 shows a schematic of the data acquisition system. Matlab, running on a PC (32 GB RAM, 3.4 GHz Intel Core™ i7-6700 processor), was used to interface with the hardware.

4.3. Thermal fatigue evaluation

In this work, changes in shear and Rayleigh wave measurements, and EBSD imaging were used to confirm the presence of thermal fatigue based on [38,39].

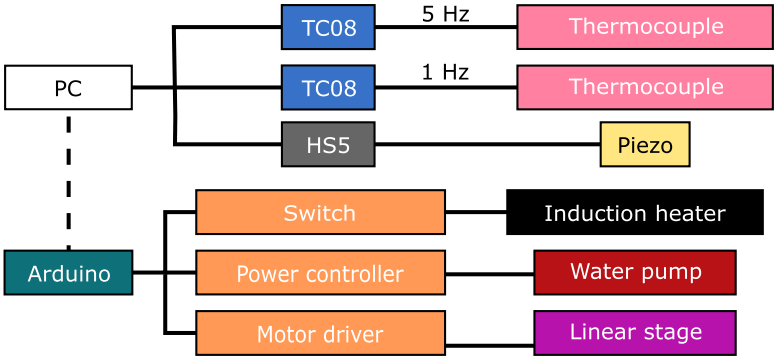


Fig. 3. Block diagram of equipment and data acquisition system connections.

Table 2
Summary of the velocity map wave polarisations measured for each sample.

Sample	Fatigue state	Shear polarisations(s)
A	Pre	0°
	Post	0°
B	Pre	0°
	Post	0° & 90°
C	Pre	0° & 90°
	Post	0° & 90°

4.3.1. Shear wave measurements

Shear wave velocity maps were obtained before and after fatiguing using a shear wave EMAT attached to a three-axis scanning frame following [38]. A custom acquisition system and Low Pull EMAT (Sonobotics, UK) were used to acquire pulse-echo signals at 3.6 MHz with a 3-cycle Hann-windowed excitation. The scanning step was 0.6 mm (≈ 0.675 shear wavelengths). For the cracked samples, the velocity maps were obtained for orthogonal shear polarisations; a summary is given in Table 2.

Each A-scan comprised 1000 averaged signals to reduce noise. The TOF was computed using parabolic auto-correlation interpolation [45]. The velocity was computed using Eq. (3) where v and τ are the velocity and TOF, whilst L is the wave propagation distance. For the pulse-echo EMAT measurements, L is twice the sample thicknesses given in Table 1 to account for the pulse-echo setup.

$$v = \frac{L}{\tau} \tag{3}$$

The change in velocity relative to the pre-fatigued state, Δv_p^*, was computed using Eq. (4) for each location p. The variables $v_{p,h}$ and $v_{p,f}$ in Eq. (4) denote the healthy and fatigued velocities, respectively. The velocity maps were computed for the 0° polarisations only.

$$\Delta v_p^* = \frac{v_{p,h} - v_{p,f}}{v_{p,h}} \tag{4}$$

Pre- and post-fatigue attenuation maps were derived from the same velocity map data using Eq. (5) where I_1 and I_2 are the first and second back-wall echo amplitudes of the A-scan envelope (obtained using the Hilbert transform [46]), respectively, whilst d is the sample thickness. The attenuation maps were computed for both shear polarisations where applicable (see Table 2).

$$A = 20\log_{10}\left(\frac{I_1}{I_2}\right) \times \frac{1}{2d} \tag{5}$$

Additionally, the average relative change in (temperature-compensated) velocity as measured by the bonded piezo was calculated over the 30 s periods of uniform temperature at the start of each test to assess the long-term variations. The temperature-compensated velocity, v_{comp}, was calculated for each specific sample using Eq. (6) where v and $v(T)$ are obtained using Eqs. (3) and (7), respectively. In Eq. (6), T is the mean temperature of the two N-type thermocouples, whilst T_0 is the mean temperature of the same two thermocouples obtained in the first test of each sample only. Both T and T_0 have units of °C.

$$v_{\text{comp}} = v - (v(T) - v(T_0)) \tag{6}$$

In Eq. (7), the coefficients P_2 and P_1 have the same values and units (taken from [41]) as stated when Eq. (1) was previously introduced. Specific values of P_0^* were calculated, in units of m s^{-1}, for each sample using TOF and temperature data acquired before any thermal cycling (to ensure near-uniform temperature conditions), and the sample thicknesses in Table 1.

$$v(T) = P_2 T^2 P_1 T + P_0^* \tag{7}$$

Attenuation, as measured by the bonded piezo, was calculated using Eq. (5). The average attenuation was computed over periods where the 100-point moving standard deviation was less than 12 dB m^{-1}. This threshold was chosen to identify either the 30 s periods of uniform temperature at the start of each test or the 15 min pauses after every 90 transients.

4.3.2. Rayleigh wave measurements

Pitch-catch Rayleigh wave measurements were performed at 5 mm increments along the 120 mm edge to compare the velocity variation between the top (fatigued) and bottom (unfatigued) surfaces of sample A after fatiguing. Two V154-RM 2.25 MHz shear contact transducers (Evident Scientific, Japan) were used, with Lyle's black treacle (Tate and Lyle, UK) serving as the couplant. A 45° angle and constant pressure between the transducers and the sample edge were maintained using the jig shown in Fig. 4. This transducer setup eliminates the need for Perspex wedges to generate Rayleigh waves, as in [39], although a strong shear wave is also expected to be generated. The setup additionally eliminates the reference measurement required by the method presented in [39].

A 5-cycle, 2.25 MHz Hann-windowed TOP sequence excitation sequence [44] was used, generated by a Handyscope HS5 (TiePie, Netherlands) sampling at 50 MHz. The TOF was computed from the average of 100 A-scans at each measurement location using parabolic auto-correlation interpolation [45]. Auto-correlation was possible because of electrical crosstalk between the arbitrary function generator and oscilloscope channels of the HS5, meaning the transmission signal appeared in the receiver transducer signal. The velocity for each measurement location was calculated using Eq. (3) where L is 40 mm to account for the pitch-catch configuration as shown in Fig. 4.

4.3.3. Electron backscatter diffraction imaging

Geometrically necessary dislocation maps in sample A were obtained for two locations, as illustrated in Fig. 5, using EBSD. Given its proximity to the heated (fatigue-damaged) surface, the dislocation density of location A-1 was expected to be higher than location A-2. The sub-samples

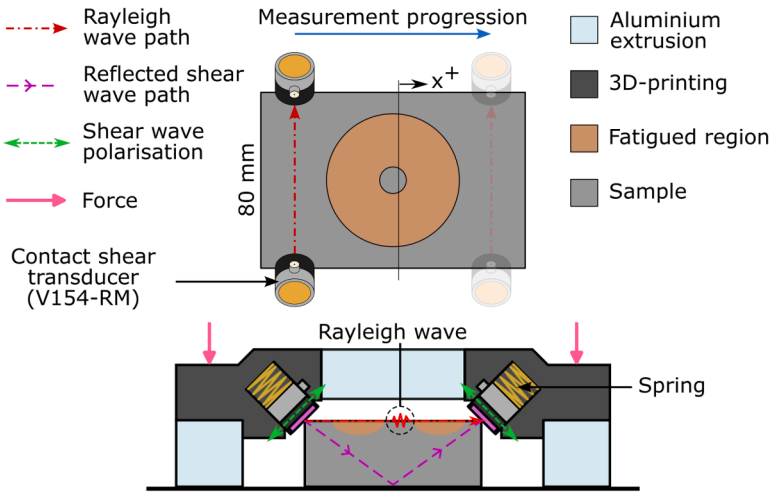


Fig. 4. Schematic of the Rayleigh wave measurement setup. Top: Rayleigh wave propagation and scan directions; transducer jig not shown for clarity. Bottom: simplified cross-section of the transducer jig used to maintain pressure and a 45° angle between the contact transducer face and the sample edge.

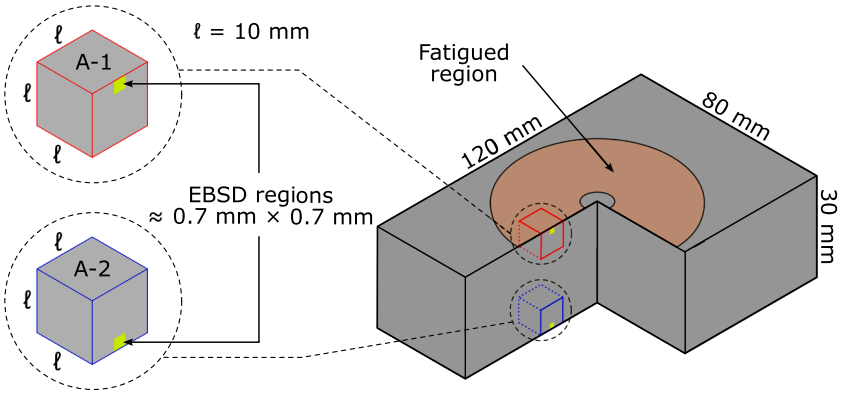


Fig. 5. Schematic illustrating the sub-samples of Sample A which contain the locations A-1 and A-2 imaged using EBSD to measure dislocation density.

were cut from sample A using wire electrical discharge machining. The sub-samples were then ground and polished following [39]: grind progressively with silicon carbide paper from 600 to 4000 grit followed by 1 µm diamond paste and oxide polishing suspension (OPS) polishing for 45 min, respectively.

Each sub-sample was placed in a Tescan Clara Scanning Electron Microscope (Brno, Czechia), in which 30 keV acceleration voltage and 10 nA current were set. The Oxford Instrument EBSD system, Symmetry 2, was used to acquire 700 µm × 700 µm EBSD images with a step size of 2 µm at 279× magnification. The dislocation density was calculated from each dislocation map.

4.3.4. Crack morphology

The top surfaces of the cracked samples (B and C) were photographed using a Canon EOS 7D DSLR camera and Canon Zoom Lens EF 24 mm–105 mm (Canon, Japan). The crack morphologies were manually traced in Inkscape [47] and superimposed on the attenuation map of each sample.

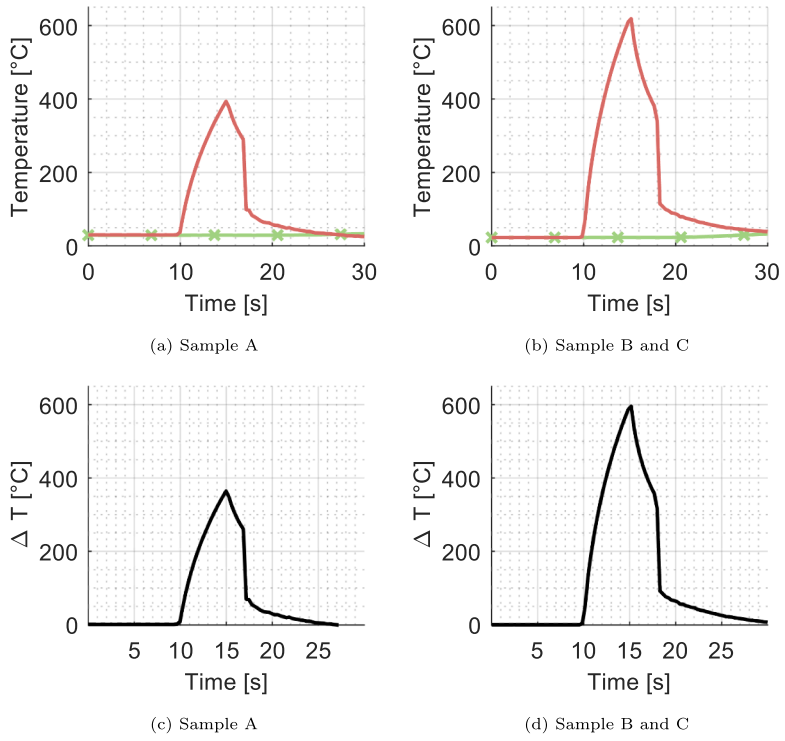
5. Results and discussion

5.1. Thermal transients

The top row of Fig. 6 shows representative examples of the thermal transients for each sample measured using the top and bottom surface thermocouples. The bottom row of Fig. 6 shows the temperature difference between the two thermocouples. The repeatability of N-type thermocouples used to obtain the data is the larger of ±2.2 °C and ± 0.75% of the values [42]. Due to the temperature magnitudes, error bars would not be visible and hence have been omitted from Fig. 6. As stated previously, the magnitudes of the thermal transients exceed those of Civaux 1. This was a deliberate choice to induce low-cycle thermal fatigue and observe damage within a reasonable time frame. It is possible to adjust the experimental setup to reduce the thermal transients and induce HCTF.

5.2. Shear wave velocity

Fig. 7 shows the change in shear wave velocity (0° shear polarisation) calculated relative to the pre-fatigued value using Eq. (4) for each sample. Each sample exhibits a clear reduction in velocity within the bounds of the induction coil, reflecting the heating pattern. The same behaviour was observed for the 90° polarisations and therefore, they are not presented. The absolute maximum reduction in velocities were ≈ 0.76%, 0.61% and 0.49% for samples A–C, respectively. Samples B and C were expected to show greater velocity changes than sample A, as their cracking implies more fatigue damage, resulting from a higher number of thermal transients in sample B and larger thermal transients in both B and C. However, sample A showed the highest absolute reduction in velocity. There are several factors which may have contributed to this result such as variations in the sample chemical compositions [39]. However, further work is required to determine the exact reasons. Furthermore, given the limited sample set, a clear quantitative relationship between velocity reduction and damage accumulation cannot be



(a) Sample A (b) Sample B and C

(c) Sample A (d) Sample B and C

Fig. 6. Top row: Representative thermal transients for each sample measured using the top and bottom surface thermocouples. Bottom row: Difference between the two thermocouples.

established. Nevertheless, the results are in line with the findings of Sarris et al. [39].

Fig. 8 shows the change in (temperature-compensated) shear wave velocity relative to the pre-fatigued state, averaged over the period of uniform temperature at the start of each test. The velocity in each sample decreased as time and the cumulative number of thermal cycles increased. The reduction in velocity is caused by the accumulation of fatigue damage (increased dislocation density) [34,40]. The cycling of sample C was halted after visual observations of cracking at ≈ 10 h, with the last period of uniform temperature occurring after ≈ 3 h of cycling (as shown in Fig. 8). The time for the onset of cracking in sample C was extremely short. Nevertheless, the results suggest that thermal fatigue damage monitoring may be feasible via continuous measurement of velocity, provided measurements can be made at a near-uniform temperature state using a permanently installed transducer.

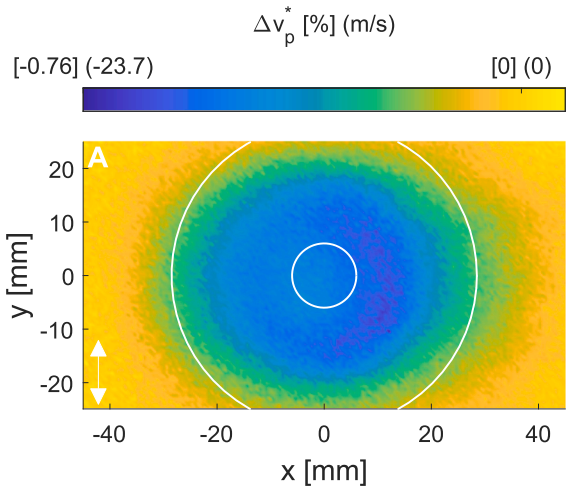
5.3. Shear wave attenuation

Figs. 9–11 show the attenuation maps of each sample pre- and post-fatiguing for each polarisation measured. For sample A, there was no significant change in attenuation after fatiguing, apart from the region in the right part of the annulus. This region corresponds to the approximate position of the piezo. The increase in attenuation may be due to increased surface roughness caused by sanding with coarse abrasive paper to remove the epoxy. However, this hypothesis was not investigated. Sanding was avoided for samples B and C, and a much larger increase in attenuation for both polarisations after fatiguing can be observed in Figs. 10 and 11. The increase in attenuation is due to the presence of the surface-breaking cracks – Fig. 18 in Section 5.6 compares the crack morphologies and attenuation maps.

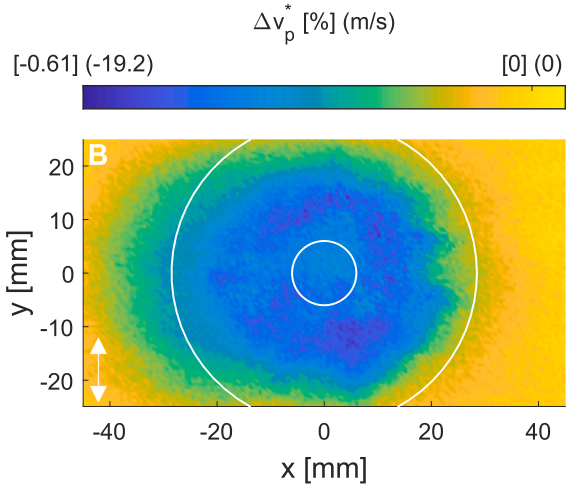
Fig. 12 shows the change in shear wave attenuation relative to the pre-fatigued state, averaged over periods where the 100-point moving standard deviation was less than $12\,\mathrm{dB\,m^{-1}}$. The x-axis of Fig. 12 simply presents the data in chronological order with uniform spacing. This effective (unitless) measure of time is a proxy for the number of cycles experienced and has been used for clarity of visualisation. In samples B and C, the attenuation generally increases as the cumulative number of thermal cycles increases. On the other hand, sample A showed a decrease in attenuation, which is in contradiction with the theory [34,40]. The cause of the decrease is unclear; however, the magnitude was less than the increase in samples B and C. The increase in attenuation for sample C is significantly larger than for sample B. This is because the piezo (and hence shear polarisation) was oriented perpendicular to the (expected) crack orientation for sample C, causing more scattering of the ultrasound compared with the parallel alignment for sample B [48]. It should be noted that the attenuation data in Fig. 12 were not temperature compensated, which likely explains the sporadic fluctuations between the attenuation values calculated during the 30 s pre-cycling period (filled markers) and the 15 min cycling pause period (unfilled markers).

Although thermal fatigue damage increases ultrasonic attenuation [34,40], the increase observed here is attributed to the development of the cracks. This is because the attenuation maps for sample A (not cracked, Fig. 9) did not show an appreciable increase pre- and post-fatiguing, whereas the maps for samples B and C (cracked, Figs. 10 and 11) did. Monitoring changes in attenuation may allow detection of the onset and progression of thermal fatigue cracking. This is supported by previous investigations of attenuation-based methods to monitor mechanical fatigue and resulting crack growth [49–53]. However, future investigations are necessary to confirm whether the detection of changes in velocity and attenuation measured by the bonded piezo is viable under thermal conditions that induce high-cycle (rather than low-cycle) thermal fatigue. For example, the Flow-Structure Interaction (FSI) facility [33].

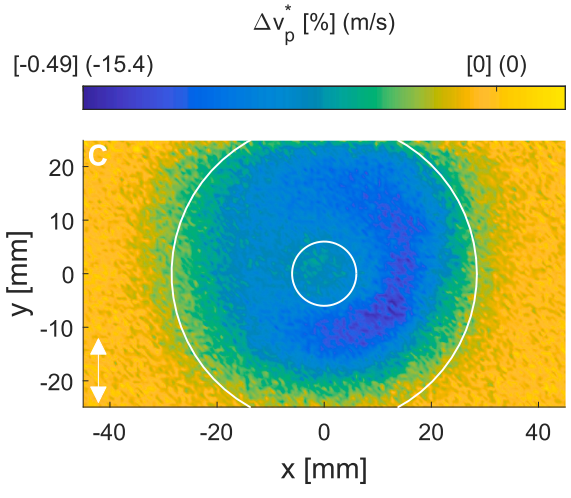
Fig. 13 shows pulse-echo signals measured using the bonded piezo on sample C at the start (0 cycles) and end (1064 cycles) of the thermal cycling. Three echoes can be seen at 0 cycles after the initial excitation; after 1064 cycles, the echoes are no longer visible, implying that the piezo or bonding deteriorated. To verify that the significant increase in attenuation observed in Fig. 12 was caused by crack development



(a) Sample A



(b) Sample B



(c) Sample C

Fig. 7. Change in shear wave velocity for each sample calculated using Eq. (4) relative to the pre-fatigue data (0° polarisation only). Induction coil bounds illustrated by the annulus. Double-headed arrows denote shear wave polarisation of the post-fatigue measurements.

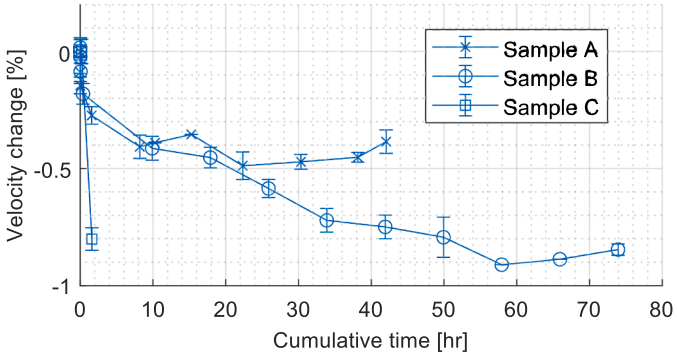
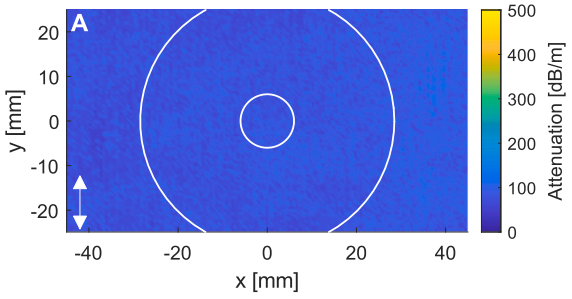
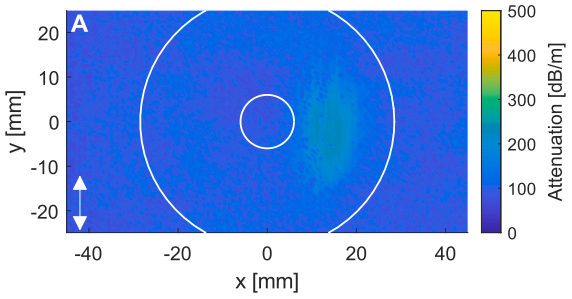


Fig. 8. Relative change in temperature-compensated (Eq. (6)) wave velocity averaged over the 30 s periods of uniform temperature at the start of each test for each sample. The error bars denote one standard deviation.



(a) Pre-fatigue.

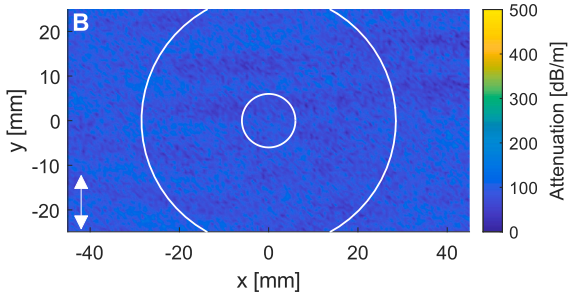


(b) Post-fatigue.

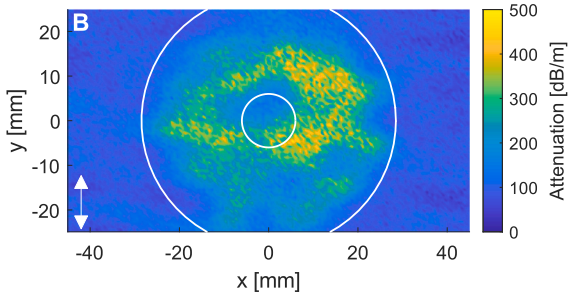
Fig. 9. Shear wave attenuation for sample A calculated using Eq. (5). Induction coil bounds illustrated by the annulus. Double-headed arrows denote shear wave polarisation.

rather than piezo or bonding deterioration, a through-thickness pitch-catch measurement was performed between the bonded piezo (transmitter) and a V154-RM 2.25 MHz shear contact transducer (receiver) after the sample was removed from the fatigue rig. The contact transducer was placed directly opposite the bonded piezo on the surface that was heated during the thermal cycling.

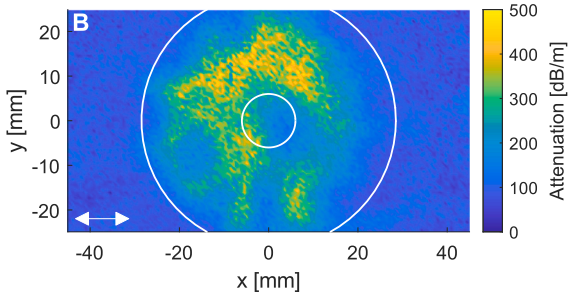
The pitch-catch A-scan is shown in Fig. 14; crosstalk between the arbitrary function generator and oscilloscope channel of the HS5 can be observed between 0 and 5 µs. The through-transmission shear wave signal can clearly be observed at ≈ 12 µs (dash-dot black line), which corresponds to approximately half of the first pulse-echo back-wall of a shear wave reflection arrival time (shown in Fig. 13) as expected. This demonstrates that the bonding was able to transmit ultrasound even after the thermal cycling. This confirms the attenuation changes observed in Fig. 12 are not (solely) due to degradation of the bonding or piezo.



(a) Pre-fatigue, 0° polarisation.



(b) Post-fatigue, 0° polarisation.

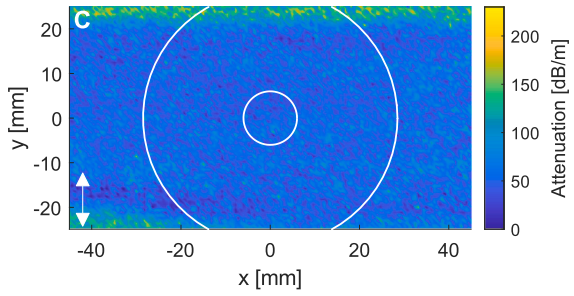


(c) Post-fatigue, 90° polarisation.

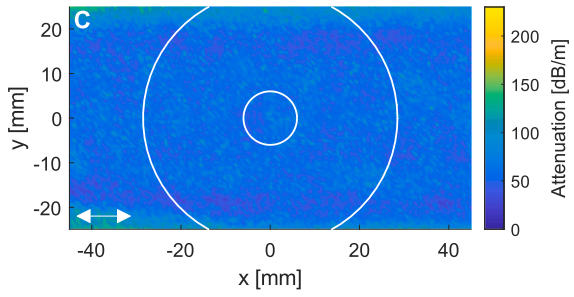
Fig. 10. Shear wave attenuation for sample B calculated using Eq. (5). Induction coil bounds illustrated by the annulus. Double-headed arrows denote shear wave polarisation.

Nevertheless, bonding degradation is a known issue even at temperatures $\leq 40\,^{\circ}\mathrm{C}$ [54]. EMATs offer a couplant-free solution to avoid couplant/bonding variability. EMATs could not be used during the thermal cycling due to electromagnetic interference from the induction heater. However, EMAT usage should be possible in the real world, as this inference is unlikely to be present and EMATs resistant to extreme temperatures exist: [55–62]. Furthermore, the orientation and size of cracks can be obtained using an orthogonal co-located coils (OCLC) shear wave EMAT [63].

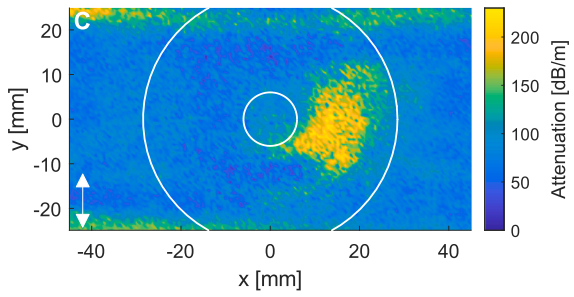
The design of the transducer and associated hardware is an important step for the successful adoption of the proposed monitoring technique. The design process should consider factors such as reliability, maintenance requirements, service life, for thermal fatigue monitoring in NPPs and more widely. This significant topic cannot be fully addressed in this work; however, these challenges are well recognised in the literature on sensing systems for challenging environments, where factors such as high temperature, radiation, corrosion, and mechanical loading significantly affect sensor stability, sensitivity, and lifespan [64]. In particular, studies on ultrasonic sensors for nuclear and high-temperature applications highlight issues related to material degradation, bonding techniques, and long-term reliability of permanently installed monitoring systems [23,65–67].



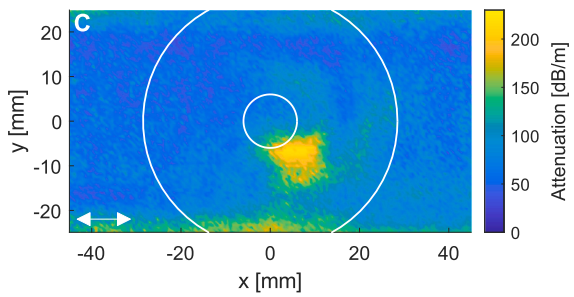
(a) Pre-fatigue, 0° polarisation.



(b) Pre-fatigue, 90° polarisation.



(c) Post-fatigue, 0° polarisation.



(d) Post-fatigue, 90° polarisation.

Fig. 11. Shear wave attenuation for sample C calculated using Eq. (5). Induction coil bounds illustrated by the annulus. Double-headed arrows denote shear wave polarisation.

5.4. Rayleigh wave velocity

Fig. 15 shows the spatial variation in the Rayleigh wave velocity on the top and bottom surfaces of sample A. The errorbars ($\Delta v \approx 2\,\mathrm{m\,s^{-1}}$) were calculated using Eq. (8) where L, $\delta\tau$ and τ are the 80 mm sample depth, 20 ns resolution of the Handyscope HS5 and the TOF calculated using parabolic interpolation of the auto-correlation, respectively.

$$\Delta v = \frac{L \cdot \delta\tau}{\tau^2} \tag{8}$$

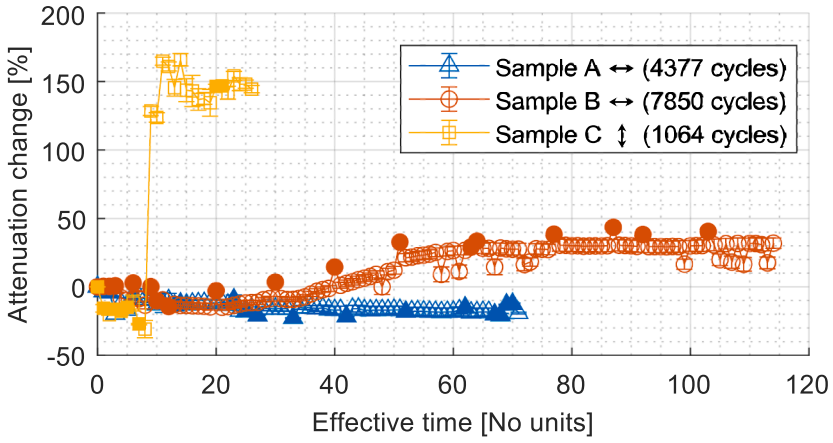


Fig. 12. Average relative change in shear wave attenuation for each sample in each test. Error bars represent one standard deviation. The x-axis shows measurements in chronological order, made contiguous for clarity. Filled and unfilled markers indicate attenuation calculated during the 30 s pre-cycling and 15 min cycling pause periods, respectively.

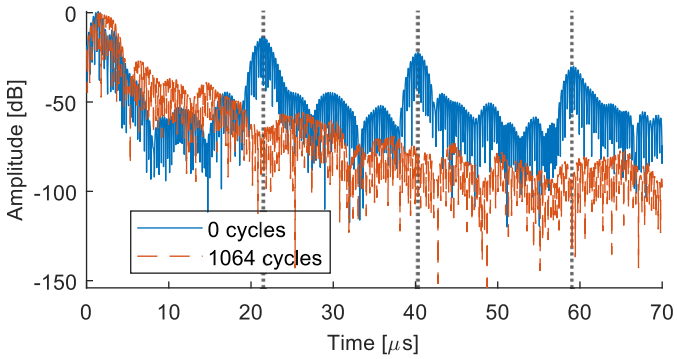


Fig. 13. Pulse-echo signals measured after 0 and 1064 thermal cycles of sample C using the bonded piezoelectric crystal. The vertical dotted lines indicate the arrival times of the first three back-wall echoes.

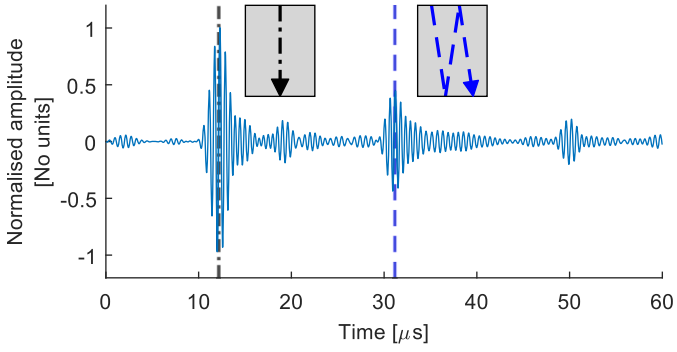


Fig. 14. Pitch-catch signal measured between the bonded piezoelectric crystal (transmitter) and a 2.25 MHz shear contact transducer (receiver) after 1064 thermal cycles of sample C. The vertical lines (Dash-dot black and dashed blue) correspond to the (shear) wave paths illustrated in the inset arrow-rectangle graphics. (For interpretation of the references to colour in this figure legend, the reader is referred to the web version of this article.)

The bottom surface showed a difference of $\approx 7\,\mathrm{m\,s^{-1}}$ between the fastest and slowest Rayleigh wave velocities. The velocity on the top surface decreased significantly within the bounds of the induction heating coil annulus. The maximum change was $\approx 86\,\mathrm{m\,s^{-1}}$ which corresponds to a 2.7% decrease compared with the average bottom surface velocity. The change in velocity is equivalent to a change of 2.5 mm in travel distance for a TOF of 29.64 μs, which far exceeds any variation in the 80 mm dimension of sample A. The top surface velocity also decreased

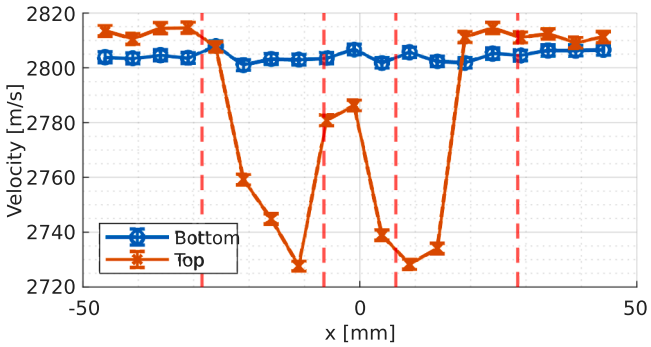


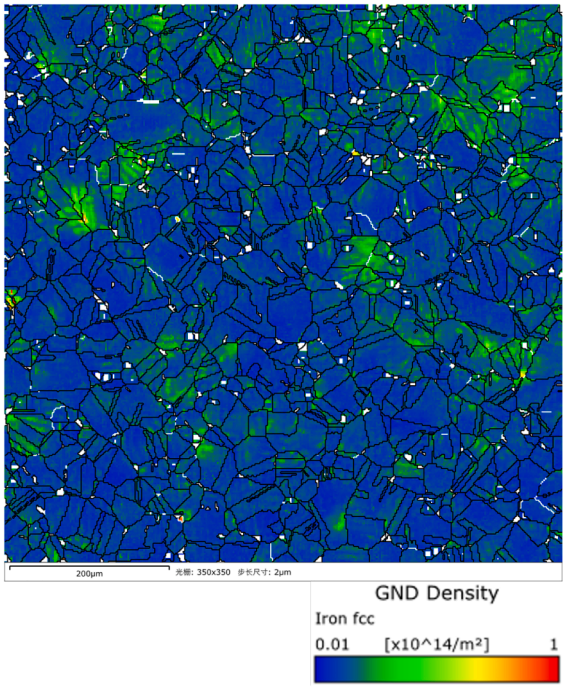
Fig. 15. B-scan showing the variation in the Rayleigh wave velocity on the top and bottom surfaces of sample A. The vertical dashed lines denote the bounds of the induction heating coil annulus.

near the centre of the sample, but by a lower amount: $28\,\mathrm{m\,s^{-1}}$. These findings align with the expectation that the top surface was fatigue-damaged whilst the bottom remained unfatigued. Furthermore, the reduced decrease in velocity close to the centre of the sample implies that the severity of fatigue damage is lower than directly under the induction coil. This is also as expected due to the reduction in the induced heating away from the induction coil. The spatial velocity variation in Fig. 15 demonstrates an improvement on the results presented by Sarris et al. [39], which did not show spatial variation in velocity.

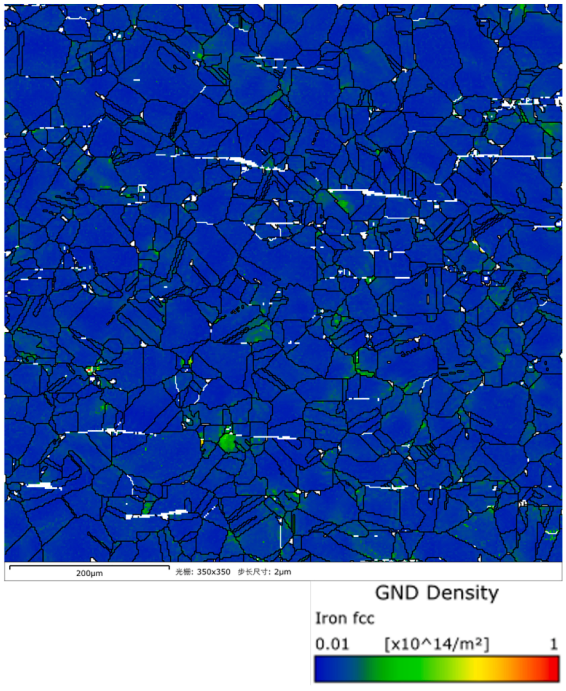
The maximum relative change in Rayleigh wave velocity (2.7%) was comparable to those reported by Sarris et al. (4%) [39]. However, the effect was observable at a wavelength of ≈ 1.2 mm (assuming a wave speed of $2804\,\mathrm{m\,s^{-1}}$) compared with ≈ 0.3 mm (10 MHz) used by Sarris et al. This implies that the fatigued layer for sample A is larger than the samples presented by Sarris et al. This may be due to differences in the steel compositions in this work and in [39].

5.5. Electron backscatter diffraction imaging

Fig. 16 show the geometrically necessary dislocation maps of subsamples A-1 and A-2. A-1 (Fig. 16(a)) shows a higher number of dislocations compared with A-2 (Fig. 16(b)). The average dislocation densities of A-1 and A-2 are $0.13 \times 10^{14}\mathrm{m}^{-2}$ and $0.09 \times 10^{14}\mathrm{m}^{-2}$, respectively based on the maps in Fig. 16. This implies that the experimental setup used in this work has induced fatigue damage and the observed ultrasonic velocity and attenuation changes can be attributed to this damage.



(a) Sub-sample A-1 (fatigued).

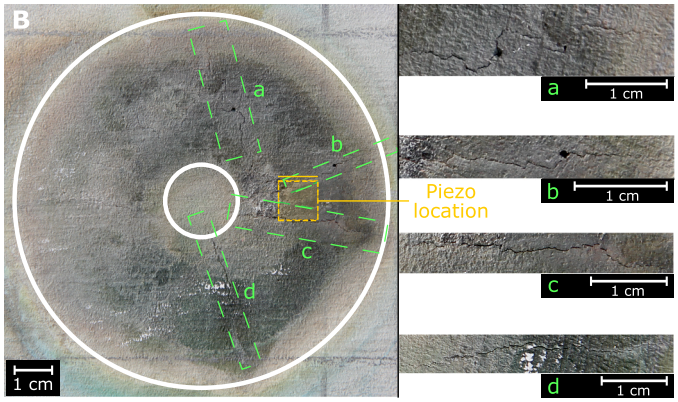


(b) Sub-sample A-2 (unfatigued).

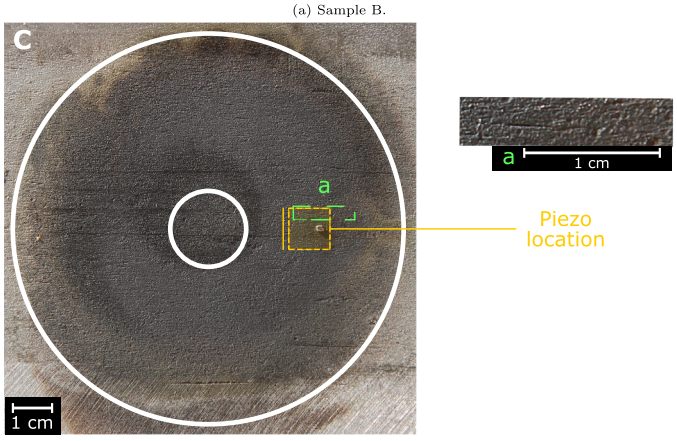
Fig. 16. Geometrically necessary dislocation maps obtained using EBSD of the sub-samples of sample A illustrated in Fig. 5.

5.6. Crack morphology

Fig. 17 shows images of the cracked surfaces of samples B and C. In both samples, the cracks are concentrated within the bounds of the induction heating coil. The crack morphologies extracted from Fig. 17(a) and (b) were superimposed on the mean of the attenuation maps at different polarisations (Figs. 10 and 11) shown in Fig. 18(a) and (b). There is good alignment between the regions of high mean polarisation attenuation with the crack morphology for sample B, but not for sample C. It is possible that additional microcracks are present in sample C, but cannot be differentiated from the rough surface using visual inspection alone. The visually observable crack in sample C is smaller in length and presumably depth than the cracks in sample B. Assuming reduced crack depth would explain the lower magnitude in maximum attenuation shown in Figs. 11(c), (d), 18(b) compared with Figs. 10(b), (c), 18(a).



(a) Sample B.



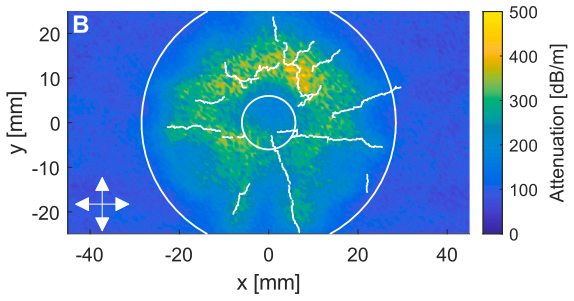
(b) Sample C.

Fig. 17. Images of the cracked surfaces. Induction coil bounds illustrated by the annulus. The dashed squares indicate the locations of the piezo. The horizontal and vertical lines near the dashed squares in panels (a) and (b), respectively, denote the shear wave polarisation. The right side of each panel shows zoomed views of selected cracks.

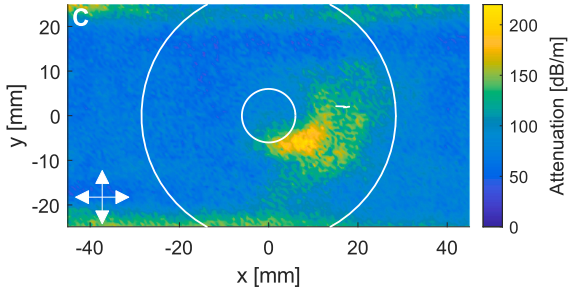
Sample C was visually inspected after each thermal cycling test for the presence of cracks; the cycling was stopped once cracks were observed after ≈ 1064 cycles. Sample B shows more cracking than sample C due to the higher number of thermal cycles. The low number of cycles to induce cracking implies that the fatigue for sample C (and presumably for sample B too) was in the low-cycle regime. This is unsurprising given the extreme temperature transients. Furthermore, the samples were tested in their as-received state; therefore, the rough surface and any residual stresses may have contributed to the acceleration of the crack initiation and growth. However, to validate these potential causes, testing of a larger number of samples is required.

5.7. Limitations of the current work

The current work suggests that continuous monitoring of ultrasonic velocity can provide an early indication of thermal fatigue damage well before failure. However, it is well established that fatigue-type problems exhibit significant statistical variation [68]. Hence, supplementary tests are required to confirm the results from the limited dataset in this work.



(a) Sample B.



(b) Sample C.

Fig. 18. Extracted crack morphologies superimposed on the mean polarisation attenuation maps of the two polarisations post-fatigue (Figs. 10 and 11).

Additionally, to demonstrate the viability of the presented method, future work should include factors such as:

1. Different thermal loading and cycle numbers to better represent HCTF fatigue conditions.
2. Simultaneous thermo-mechanical loading to better represent real-world conditions.
3. In-service interferences including flow-induced corrosion, neutron irradiation and mechanical vibration.
4. Sample condition e.g., surface roughness and chemical composition including other grades of carbon and stainless steel susceptible to thermal fatigue damage [12].
5. Sample geometry.

Another aspect that should be addressed in future work is the influence of thermal gradients and dynamic temperature variations. The presented method requires periods of near-uniform thermal conditions which may not be realistic. A technique to correct for spatial temperature inhomogeneity will improve damage detection accuracy. Previous work by the authors have investigated potential physics- and machine learning-based techniques to address this issue [69,70].

Finally, it should be highlighted that the literature shows the spatial distribution of HCTF damage can vary significantly depending on flow conditions such as turbulence and pipe geometry [14,71–77]. Therefore, a network or array of measurement points will likely be required to allow spatial coverage of damage progression. This may have the added benefit of enabling imaging for quantifying crack size, location or orientation.

6. Conclusion

In this work, experiments were performed using a bespoke setup capable of creating non-homogeneous thermal transients up to 600 °C in 30 mm-thick samples of 304 SS via induction heating and water cooling. The thermal transients were used to induce (low-cycle) thermal fatigue in the samples. Shear wave piezos were bonded to the samples to monitor long-term changes in the ultrasonic velocity and attenuation caused by the thermal cycling.

Thermal fatigue damage was achieved in all the samples (including cracking in two of the samples). The presence of thermal fatigue damage was confirmed using EBSD imaging, shear wave velocity maps and Rayleigh wave measurements based on [38–40]. Analysis of the ultrasonic signals from permanently bonded piezos suggests that tracking the progression of thermal fatigue damage is possible by using the long-term variation in the shear wave velocity and attenuation, respectively, measured during periods of uniform temperature. This method corroborates the findings by Sarris et al. [38–40] and overcomes the thermal filtering limitation suffered by temperature-based monitoring methods. However, a larger campaign of testing is paramount to confirm efficacy.

CRediT authorship contribution statement

Laurence Clarkson: Writing – review & editing, Writing – original draft, Visualization, Validation, Software, Methodology, Investigation, Formal analysis, Data curation, Conceptualization; **Frederic Cegla:** Writing – review & editing, Supervision, Resources, Project administration, Methodology, Investigation, Funding acquisition, Formal analysis, Conceptualization.

Data availability

Data will be made available on request.

Declaration of competing interest

The authors declare that they have no known competing financial interests or personal relationships that could have appeared to influence the work reported in this paper.

Acknowledgement

The authors acknowledge project funding from EPSRC as part of the FIND CDT (EP/S023275/1). They also thank Antonio De-Sanctis and Liam Corette for technical support, Connor Challinor for the TOP sequence code, Dr Stefano Galvan for advice on the data acquisition code, Paddy Caskey for assistance with the Sonobotics acquisition system, and Guotong Zou for assistance in obtaining the EBSD images.

References

[1] J. Couturier, M. Schwarz, Current State of Research on Pressurized Water Reactor Safety, EDP Sciences, 2018. https://www.edp-open.org/books/edp-open-books/349-current-state-of-research-on-pressurized-water-reactor-safety.
[2] World Information Service on Energy, France: Serious accident at Civaux-1, Nuclear Monitor Issue: #495, 1998, https://www.wiseinternational.org/nuclear-monitor/495/france-serious-accident-civaux-1.
[3] Y. Bouveret, J.M. Tchilian, G. Theron, O. de Vareilles, Detection of thermal fatigue cracks in stainless steel pipe: application to the inspection of RHRS line of type N4/PWR, in: 15th World Conference on Non Destructive Testing, Associazione Italiana Prove Non Distruttive, 2000. https://www.ndt.net/article/wcndt00/papers/idn416/idn416.htm.
[4] S. Basu, A.K. Debnath, Chapter 2 - Main Equipment, Academic Press, Boston, 2nd edition, 2019, pp. 41–147. https://doi.org/10.1016/B978-0-12-819504-8.00002-0
[5] G.E. Dieter, Mechanical Metallurgy, McGraw-Hill, 1961. https://archive.org/details/mechanicalmetall00diet/page/334/mode/2up.
[6] G.S. Was, S. Ukai, Austenitic Stainless Steels, Elsevier, 2019. https://doi.org/10.1016/B978-0-12-397046-6.00008-3
[7] P.J. Maziasz, J.T. Busby, Properties of austenitic steels for nuclear reactor applications, Elsevier, Oxford, 2nd edition, 2020, pp. 303–318. https://doi.org/10.1016/B978-0-12-803581-8.11736-9
[8] NEA, NEA CODAP Project Topical Report: A Review of the "Post-1998" Experience with Thermal Fatigue in Heavy Water and Light Water Reactor Piping Components, Technical Report NEA/CSNI/R(2019)13, NEA, 2022.
[9] M.F. Cipière, J.A. Le Duff, Thermal fatigue experience in French piping: influence of surface condition and weld local geometry, Weld. World 46 (2002). https://doi.org/10.1007/BF03266362

[10] C. Faidy, T.L. Courtois, E. de Fraguier, J.-A. Leduff, A. Lefrançois, J. Dechelotte, Thermal fatigue in French RHR system, in: EPRI (Ed.), Proceedings of the 2000 International Conference on Fatigue of Reactor Components (MRP-46): PWR Materials Reliability Program (PWRMRP), 2001, pp. 155–166. https://www.epri.com/research/products/1006070.
[11] E. Molinie, N. Monteil, S. Delatouche, S. Roux, N. Robert, C. Pagés, Caractérisation des tronçons RRA (Circuit de refrigeration du reacteur a l'arret) 900–1300 MWe deposés: synthese des enseignements, in: Proceedings of International Symposium on Contribution of Materials Investigations to the Resolution of Problems Encountered in Pressurized Water Reactors, 2002, pp. 883–895.
[12] M. Dahlberg, D. Chapuliot, I. Bretherton, C. Faidy, M. Church, S. Chapuliot, U. Wilke, N. Taylor, J. Solin, K.-F. Nilsson, J. Catalano, Development of a European Procedure for Assessment of High Cycle Thermal Fatigue in Light Water Reactors: Final Report of the NESC-Thermal Fatigue Project, Technical Report LD-NA-22763-EN-C, Institute for Energy and Transport (Joint Research Centre), 2007. https://op.europa.eu/s/y0vU.
[13] J.I. Lee, L.-W. Hu, P. Saha, M.S. Kazimi, Numerical analysis of thermal striping induced high cycle thermal fatigue in a mixing tee, Nucl. Eng. Des. 239 (2009) 833–839. https://doi.org/10.1016/j.nucengdes.2008.06.014
[14] O.C. Garrido, S. El Shawish, L. Cizelj, Stress assessment in piping under synthetic thermal loads emulating turbulent fluid mixing, Nucl. Eng. Des. 283 (2015) 114–130. https://doi.org/10.1016/j.nucengdes.2014.10.016
[15] I. de Radioprotection et, IRSN's Position on Safety and Radiation Protection at Nuclear Power Plants in France in 2013, Technical Report, Institut de radioprotection et de sûreté nucléaire, 2014. https://www.irsn.fr/EN/publications/technical-publications/Documents/IRSN-Report_Safety-Radiation-Protection-NPP-France-2013.pdf.
[16] Autorité de sûreté nucléaire, Stress corrosion: presence of a deep crack on the safety injection system of reactor 1 of the Penly nuclear power plant [Update], 2023, https://www.french-nuclear-safety.fr/information/news-archives/stress-corrosion-penly-nuclear-power-plant.
[17] Autorité de sûreté nucléaire et de radioprotection, Inspection strategy for stress corrosion cracking (SCC) for the years 2023 to 2025, 2023, (https://www.french-nuclear-safety.fr/content/download/188720/file/Inspection%20strategy%20for%20stress%20corrosion%20cracking%20(SCC)%20for%20the%20years%202023%20to%202025.pdf). Letter reference: CODEP-DEP-2023-007194.
[18] M. Mitra, S. Gopalakrishnan, Guided wave based structural health monitoring: a review, Smart Mater. Struct. 25 (2016) 53001. https://doi.org/10.1088/0964-1726/25/5/053001
[19] S.K. Bussa, N.K. Boppana, K. Gunda, A literature review of approaches to structural integrity assessment using FBG and PZT sensors, Discov. Sens. 1 (2025) 15. https://doi.org/10.1007/s44397-025-00015-z
[20] C.R. Farrar, K. Worden, Structural Health Monitoring : A Machine Learning Perspective, Wiley, 2013.
[21] H. Sohn, C.R. Farrar, F.M. Hemez, J.J. Czarnecki, A review of structural health review of structural health monitoring literature 1996–2001, Los Alamos National Laboratory, 2002. https://www.osti.gov/biblio/976152.
[22] V. Giurgiutiu, Structural Health Monitoring with Piezoelectric Wafer Active Sensors, Elsevier, 2014. https://doi.org/10.1016/C2013-0-00155-7
[23] R. Kazys, V. Vaskeliene, High temperature ultrasonic transducers: a review, Sensors 21 (2021) 3200. https://doi.org/10.3390/s21093200
[24] J. Daw, M. Good, R. Meyer, P. Ramuhalli, L. Breon, Assessment of Acoustic Sensor Application to Structural Health Monitoring of Reactor Components, Technical Report INL/RPT-23-70721, Idaho National Laboratory, Idaho Falls, ID, USA, 2022. https://inldigitallibrary.inl.gov/sites/sti/sti/Sort_64704.pdf.
[25] V. Radu, E. Paffumi, N. Taylor, K.F. Nilsson, A study on fatigue crack growth in the high cycle domain assuming sinusoidal thermal loading, Int. J. Press. Vessels Pip. 86 (2009) 818–829. https://doi.org/10.1016/j.ijpvp.2009.10.007
[26] J. Taler, P. Dzierwa, M. Jaremkiewicz, D. Taler, K. Kaczmarski, M. Trojan, T. Sobota, Thermal stress monitoring in thick walled pressure components of steam boilers, Energy 175 (2019) 645–666. https://doi.org/10.1016/j.energy.2019.03.087
[27] J. Rudolph, S. Bergholz, B. Heinz, B. Jouan, AREVA fatigue concept - a three stage approach to the fatigue assessment of power plant components, in: S.H. Chang (Ed.), Nuclear Power Plants, IntechOpen, Rijeka, 2012. https://doi.org/10.5772/37029
[28] S. Bergholz, B. Jouan, J. Rudolph, B. Heinz, Automatic fatigue monitoring based on real loads and consideration of EAF: live demonstration, in: Proceedings of the ASME 2013 Pressure Vessels and Piping Conference. Volume 1A: Codes and Standards, American Society of Mechanical Engineers, 2013, pp. 1–13. https://doi.org/10.1115/PVP2013-97236
[29] Y. Murakami, Stress Concentration, Academic Press, 2nd, 2019, pp. 13–27. https://doi.org/10.1016/B978-0-12-813876-2.00002-9
[30] M. Weikert-Müller, F. Weber, S. Thieltges, M. Smaga, F. Silber, J. Rudolph, S. Bergholz, E. Bechtgold, Development of a new thermo-mechanical load and fatigue monitoring approach based on electromagnetic acoustic transducers - EMUS-4-STRESS, in: Volume 1: Codes & Standards, American Society of Mechanical Engineers, 2023. https://doi.org/10.1115/PVP2023-107274
[31] L. Clarkson, Y. Zhang, F. Cegla, A comparison of ultrasonic temperature monitoring using machine learning and physics-based methods for high-cycle thermal fatigue monitoring, Struct. Health Monit. (2023). https://doi.org/10.1177/14759217231190041
[32] O.C. Garrido, L. Cizelj, S.E. Shawish, The role of the axial heat fluxes in the thermal fatigue assessment of piping, Nucl. Eng. Des. 261 (2013) 382–393. https://doi.org/10.1016/j.nucengdes.2013.01.024
[33] University of Stuttgart, Flow-structure interaction, 2026, https://www.ike.uni-stuttgart.de/en/research/fluidstructureinteraction/.
[34] A. Granato, K. Lücke, Theory of mechanical damping due to dislocations, J. Appl. Phys. 27 (1956) 583–593. https://doi.org/10.1063/1.1722436
[35] A. Maurel, J.-F. Mercier, F. Lund, Elastic wave propagation through a random array of dislocations, Phys. Rev. B 70 (2004) 24303. https://doi.org/10.1103/PhysRevB.70.024303
[36] A. Maurel, V. Pagneux, F. Barra, F. Lund, Wave propagation through a random array of pinned dislocations: velocity change and attenuation in a generalized Granato and Lücke theory, Phys. Rev. B 72 (2005) 174111. https://doi.org/10.1103/PhysRevB.72.174111
[37] A. Maurel, V. Pagneux, F. Barra, F. Lund, Interaction between an elastic wave and a single pinned dislocation, Phys. Rev. B 72 (2005) 174110. https://doi.org/10.1103/PhysRevB.72.174110
[38] G. Sarris, S.G. Haslinger, P. Huthwaite, M.J.S. Lowe, Fatigue state characterization of steel pipes using ultrasonic shear waves, IEEE Trans. Ultrason. Ferroelectr. Freq. Control 70 (2023) 72–80. https://doi.org/10.1109/TUFFC.2022.3226502
[39] G. Sarris, S.G. Haslinger, P. Huthwaite, M.J.S. Lowe, Ultrasonic methods for the detection of near surface fatigue damage, NDT E Int. 135 (2023). https://doi.org/10.1016/j.ndteint.2023.102790
[40] G. Sarris, Ultrasonic Methods for Assessing Fatigue Degradation in Metals, 2022, Ph.D. thesis. https://doi.org/10.25560/102892
[41] A. Gajdacsi, High Accuracy Ultrasonic Degradation Monitoring, 2015, Ph.D. thesis. https://doi.org/10.25560/55164
[42] National Institute of Standards and Technology, Temperature-Electromotive Force Reference Functions and Tables for the ITS-90, Technical Report NIST Monograph 175, U.S. Government Printing Office, Washington, DC, 1993.
[43] International Organization for Standardization, Non-destructive testing — Ultrasonic testing — Vocabulary, 3rd edition, 2025, September, ISO, Geneva.
[44] C. Challinor, N. Pearson, F. Cegla, Coded excitation using TOP-CS sequences for multi-channel low-power ultrasonics, Mech. Syst. Signal Process. 213 (2024). https://doi.org/10.1016/j.ymssp.2024.111339
[45] E. Jacobsen, P. Kootsookos, Fast, accurate frequency estimators [DSP Tips & Tricks], IEEE Signal Process. Mag. 24 (2007) 123–125. https://doi.org/10.1109/MSP.2007.361611
[46] H. Luo, X. Fang, B. Ertas, Hilbert transform and its engineering applications, AIAA J. 47 (4) (2009) 923–932. https://doi.org/10.2514/1.37649
[47] B. Harrington et al., Inkscape (v. 1.4), 2024, http://www.inkscape.org/.
[48] J. Parra-Raad, P. Khalili, F. Cegla, Shear waves with orthogonal polarisations for thickness measurement and crack detection using EMATs, NDT E Int. 111 (2020). https://doi.org/10.1016/j.ndteint.2019.102212
[49] M. Hirao, H. Ogi, N. Suzuki, T. Ohtani, Ultrasonic attenuation peak during fatigue of polycrystalline copper, Acta Mater. 48 (2000) 517–524. https://doi.org/10.1016/S1359-6454(99)00346-8
[50] H. Ogi, T. Hamaguchi, M. Hirao, Ultrasonic attenuation peak in steel and aluminum alloy during rotating bending fatigue, Metall. Mater. Trans. A 31 (2000) 1121–1128. https://doi.org/10.1007/s11661-000-0107-1
[51] T. Ohtani, H. Ogi, Y. Minami, M. Hirao, Ultrasonic attenuation monitoring of fatigue damage in low carbon steels with electromagnetic acoustic resonance (EMAR), J. Alloys Compd. 310 (2000) 440–444. https://doi.org/10.1016/S0925-8388(00)00956-7
[52] S. Kenderian, T.P. Berndt, R.E. Green, B.B. Djordjevic, Ultrasonic monitoring of dislocations during fatigue of pearlitic rail steel, Mater. Sci. Eng. A 348 (2003) 90–99. https://doi.org/10.1016/S0921-5093(02)00636-6
[53] I.M. Nurul, Y. Arai, W. Araki, Use of ultrasonic back-reflection intensity for predicting the onset of crack growth due to low-cycle fatigue in stainless steel under block loading, Ultrasonics 56 (2015) 354–360. https://doi.org/10.1016/j.ultras.2014.09.001
[54] V.A. Attarian, F.B. Cegla, P. Cawley, Long-term stability of guided wave structural health monitoring using distributed adhesively bonded piezoelectric transducers, Struct. Health Monit. 13 (2014) 265–280. https://doi.org/10.1177/1475921714522842
[55] S.S. Lee, B.Y. Ahn, Emat application at high temperature, Nondestruct. Test. Eval. 7 (1992) 253–261. https://doi.org/10.1080/10589759208953004
[56] F. Hernandez-Valle, S. Dixon, Initial tests for designing a high temperature EMAT with pulsed electromagnet, NDT E Int. 43 (2010) 171–175. https://doi.org/10.1016/j.ndteint.2009.10.009
[57] J.F. Hernandez-Valle, Pulsed-Electromagnet EMAT for High Temperature Applications, Ph.D. thesis, University of Warwick, 2011.
[58] B. Herdovics, Torsional Guided Wave EMAT for Pipeline Monitoring, Ph.D. thesis, Imperial College London, 2018.
[59] G. Zhai, B. Liang, X. Li, Y. Ge, S. Wang, High-temperature EMAT with double-coil configuration generates shear and longitudinal wave modes in paramagnetic steel, NDT E Int. 125 (2022) 102572. https://doi.org/10.1016/j.ndteint.2021.102572
[60] N. Lunn, S. Dixon, M.D.G. Potter, High temperature EMAT design for scanning or fixed point operation on magnetite coated steel, NDT E Int. 89 (2017) 74–80. https://doi.org/10.1016/j.ndteint.2017.04.001
[61] T. Zou, W. Shi, C. Lu, B. Hu, F. Qiu, Y. Liu, An improved design of high-signal-to-noise ratio spiral-coil EMAT for high-temperature defect detection, Nondestruct. Test. Eval. 40 (2025) 2982–3003. https://doi.org/10.1080/10589759.2024.2389953
[62] N. Suresh, P. Elliott, C. Radu, J. Corcoran, The design of high temperature EMATs to avoid irreversible magnetic losses, NDT E Int. 150 (2025) 103279. https://doi.org/10.1016/j.ndteint.2024.103279
[63] J. Parra-Raad, B. Lan, F. Cegla, Orthogonally polarised shear waves for evaluating anisotropy and cracks in metals, NDT E Int. 121 (2021) 102440. https://doi.org/10.1016/j.ndteint.2021.102440

[64] Q. Liu, Y. Wang, F. Zhao, C. Zheng, J. Xie, A review of the research progress of sensor monitoring technology in harsh engineering environments, Sensors 25 (2025) 6308. https://doi.org/10.3390/s25206308
[65] A.N. Sinclair, R. Malkin, Sensors for ultrasonic nondestructive testing (NDT) in harsh environments, Sensors 20 (2020) 456. https://doi.org/10.3390/s20020456
[66] B.R. Tittmann, C.F.G. Batista, Y.P. Trivedi, C.J. Lissenden, B.T. Reinhardt, State-of-the-art and practical guide to ultrasonic transducers for harsh environments including temperatures above 2120 °F (1000 °C) and neutron flux above 1013 n/cm2, Sensors 19 (2019) 4755. https://doi.org/10.3390/s19214755
[67] L. Pucci, R. Raillon, L. Taupin, F. Baqué, Design of a phased array EMAT for inspection applications in liquid sodium, Sensors 19 (2019) 4460. https://doi.org/10.3390/s19204460
[68] N.E. Dowling, Mechanical Behavior of Materials : Engineering Methods for Deformation, Fracture, and Fatigue, Pearson, 4th edition, 2013, pp. 449–451.
[69] L. Clarkson, Y. Zhang, F. Cegla, A comparison of ultrasonic temperature monitoring using machine learning and physics-based methods for high-cycle thermal fatigue monitoring, Struct. Health Monit. 23 (2024) 1560–1577. https://doi.org/10.1177/14759217231190041
[70] L. Clarkson, F. Cegla, Limitations of the 1D inverse thermal modelling method for ultrasonic thermometry, Ultrasonics 163 (2026) 107981. https://doi.org/10.1016/j.ultras.2026.107981
[71] Y. Zhang, T. Lu, Study of the quantitative assessment method for high-cycle thermal fatigue of a T-pipe under turbulent fluid mixing based on the coupled CFD-FEM method and the rainflow counting method, Nucl. Eng. Des. 309 (2016) 175–196. https://doi.org/10.1016/j.nucengdes.2016.09.021
[72] M. Kamaya, A. Nakamura, Thermal stress analysis for fatigue damage evaluation at a mixing tee, Nucl. Eng. Des. 241 (8) (2011) 2674–2687. https://doi.org/10.1016/j.nucengdes.2011.05.029
[73] K. Miyoshi, M. Kamaya, Y. Utanohara, A. Nakamura, An investigation of thermal stress characteristics by wall temperature measurements at a mixing tee, Nucl. Eng. Des. 298 (2016) 109–120. https://doi.org/10.1016/j.nucengdes.2015.12.004
[74] F. Blom, M. Church, S. Willemsen, Simplified method to predict thermal fatigue in mixing tees of nuclear reactors, in: International Conference on Fatigue Design, Cetim, 2007, p. 124.
[75] M.H.C. Hannink, A. Timperi, Simplified methods to assess thermal fatigue due to turbulent mixing, in: B.K. Dutta, R.K. Singh, P.V. Durgaprasad (Eds.), 21st International Conference on Structural Mechanics in Reactor Technology 2011 (SMiRT 21), 1, International Assn for Structural Mechanics in Reactor Technology, 2011. https://www.lib.ncsu.edu/resolver/1840.20/43774.
[76] O.C. Garrido, S.E. Shawish, L. Cizelj, A novel approach to generate random surface thermal loads in piping, Nucl. Eng. Des. 273 (2014) 98–109. https://doi.org/10.1016/j.nucengdes.2014.02.027
[77] M.H.C. Hannink, A coupled CFD-FEM strategy to predict thermal fatigue in mixing tees of nuclear reactors, 2008. https://api.semanticscholar.org/CorpusID:29766432.